Promoting effect of Ce and Mg cations in Ni/Al catalysts prepared from hydrotalcites for the dry reforming of methane

**B. Djebarri · V. M. Gonzalez-Delacruz · D. Halliche ·
K. Bachari · A. Saadi · A. Caballero ·
Juan P. Holgado · O. Cherifi**

Abstract Several catalytic systems containing Ni/Mg/Al/Ce were synthesized from nitrates of Ni^{2+}, Mg^{2+}, Al^{3+} and Ce^{3+} cations with $M^{2+}/M^{3+} = 2$ ratios by means of the carbonate co-precipitation method and subsequent calcination at 800 °C. Atomic absorption spectroscopy, X-ray diffraction (XRD), FT-IR spectroscopy, BET, temperature programmed reduction and scanning electron microscopy were used in order to describe the structural, morphological and surface characteristics of the solids completely. The effect of substitution/incorporation of Al by Ce and/or Mg on NiAl sample was studied. XRD analyses confirm that on Al-containing samples (NiAl, NiMgAl), the formation of the precursors layered double hydroxide structure. On the other hand, on cerium containing samples (NiCe, NiMgCe), poorly resolved diffractograms were observed what can be explained by the large radius of cerium. The catalysts were evaluated in the reaction of CO_2 reforming of methane at 750 °C. NiCe and NiMgAl catalysts exhibit higher activity and a H_2/CO ratio of almost 1. NiAl and NiMgCe samples showed lower conversions and a CH_4/CO_2 ratio <1, indicating the occurrence of reverse water gas shift reaction.

B. Djebarri · D. Halliche · A. Saadi · O. Cherifi
Laboratoire de Chimie du Gaz Naturel, Faculté de Chimie, USTHB, BP32, El-Alia, Alger, Algeria

V. M. Gonzalez-Delacruz · A. Caballero · J. P. Holgado
Instituto de Ciencia de Materials de Sevilla and Departamento de Quimica Inorganica,
CSIC-University of Sevilla, Avda. Americo Vespucio, 49, 41092 Seville, Spain

K. Bachari (✉)
Centre de Recherches Scientifiques (CRAPC), BP 248, 16004 Alger, Algeria
e-mail: bachari2000@yahoo.fr

Introduction

The reaction of methane reforming with carbon dioxide ($CH_4 + CO_2 \leftrightarrow 2H_2 + 2CO$) is not only of great practical interest, but also has important environmental implications: this process employs methane and carbon dioxide, two main components of green house gases and its application could lead to the reduction of their emissions to the atmosphere [1].

As in the case of the steam reforming reaction, this reaction is dreamed to be industrially catalyzed by Ni supported catalysts [2, 3], which are preferred over catalysts based on noble metals due to their lower cost and larger availability [4].

However, the Ni catalysts show high tendency to deactivation by coke deposition [5, 6]. In the last years, great efforts have been devoted to minimizing this tendency toward carbon formation on Ni catalysts. One of the possible strategies is to obtain Ni catalyst with very small nickel particles, less prone to coke deposition [7]. Among different preparation methods proposed to obtain those small Ni particles, it is noteworthy to remark the preparation of precursor materials where nickel is homogeneously distributed in an oxidic matrix (perovskites, hydrotalcites,…), which is later transformed by calcination and-or reduction steps that lead to extraction of small Ni particles distributed into an MO_x oxidic support (generally described as solid phase cristallisation method, spc) [8, 9].

In this context, the use of substitution hydrotalcites have been proposed to obtain catalysts with these enhanced properties [6, 10].

Hydrotalcites (Layered Double Hydroxides, LDH) are formed by metal hydroxide layers (brucite-type) with compensating anions and water molecules in the interlayer region, general formula: $[M^{2+}_{1-x}M^{3+}_x(OH)_2]^{x+}(A_{x/n})^{n-}\cdot mH_2O$, contain various cations (M^{2+} and M^{3+}) and anion (A^{n-}) [11].

Hydrotalcites can be prepared with several reducible cations in the structure together with the classical ones (Mg and Al) serving as precursors for the preparation of different mixed oxides which have been claimed to have high thermal stability and high performance in hydrocarbon reforming reactions [12–14].

The co-precipitation technique has been widely used to obtain hydrotalcite precursors that are later transformed into oxides with homogeneous morphological composition, which promotes a strong surface interaction between the active phase (nickel in our case) and the support retarding the sintering of the active phase during the catalytic processes and maintaining the desired small particle size. Different authors have employed the co-precipitation technique to obtain hydrotalcite-type precursors of Ni, Mg and Al, obtaining materials with excellent catalytic behavior in methane dry reforming reaction [10, 15, 16].

In the same context of inhibiting coke formation, it is interesting to mention the use of promoters with basic and redox characteristics [17, 18], cerium is one of the most used among these promoters. Ce-promoted catalysts with the presence of transition metals have attracted increasing attention in recent years due to their enhanced oxygen storage capability [19–21]. In addition, it is well known that in cerium oxide, the elimination of lattice oxygen under reducing conditions leads to the creation of anionic vacancies (CeO_{2-x}) correlated to high lattice oxygen mobility, but also known as reactive sites on the surfaces of metal oxides [22]. In

addition, metallic catalysts promoted with cerium are interesting due to improved mechanic and thermal resistance of support, higher metallic dispersion and in general better catalytic performance, and lower carbon content [23].

In previous works, Daza et al. [24–28] reported the beneficial effect of Ce-promoted catalysts prepared from hydrotalcites precursors in dry reforming of methane under severe reaction parameters, as their high activity and stability under drastic conditions of reaction and long operation times.

Considering those aspects, the purpose of this work is to investigate the effect of substitution/incorporation of Al by Ce and/or Mg on NiAl catalysts to obtain NiCe, NiMgAl and NiMgCe samples. Coprecipitation with carbonate ion as compensating anions is the preparation method in all the cases. These catalysts were characterized in order to study the structural, morphological and surface characteristics of the solids and its influence on catalysts stability and catalytic activity/selectivity in the reaction of CO_2 reforming of methane.

Experimental

Catalysts synthesis

Several systems containing Ni/Mg/Al/Ce were synthesized from nitrates of Mg^{2+}, Al^{3+}, Ni^{2+} and Ce^{3+} cations with $M^{2+}/M^{3+} = 2$ ratios. The nitrate solution was added dropwise to an aqueous solution of sodium carbonate, which was preheated to 60 °C. During co-precipitation, the slurry was vigorously stirred while keeping pH at 11 by slow addition of a diluted solution of NaOH. After complete addition of the metal nitrate solution, the suspension was stirred at 60 °C for 1 h, followed by aging at the same temperature for 18 h (without stirring). Afterwards, the solid was washed with deionized water several times until the elution liquid presented a pH equal to 7, and then dried in an oven at 60 °C for 12 h. The dried solid was ground into a fine powder that was further calcined in air at 800 °C (using a ramp of 4 °C/min) for 6 h to produce the corresponding mixed oxides ($Ni_{0.66}Al_{0.34}$, $Ni_{0.36}Mg_{0.32}Al_{0.32}$, $Ni_{0.66}Ce_{0.34}$, $Ni_{0.36}Mg_{0.34}Ce_{0.31}$), denoted as NiAl, NiMgAl, NiCe and NiMgCe.

Sample characterization

The chemical composition of the samples was determined by inductive coupling plasma-atomic emission spectroscopy (ICP-AES). Analyses were performed with a Horiba Jobin–Yvon, Ultima2 spectrometer.

Samples were analyzed by isothermal nitrogen adsorption using standard BET and BJH methods for the specific surface area and pore size distribution calculations. Measurements were carried out on a Micromeritics ASAP 2010 system. Prior to each experiment, samples were degassed at 150 °C under vacuum for 2 h.

XRD powder analyses were carried out using a Siemens D-501 equipment, with a Bragg–Brentano configuration, using CuK_α ($\lambda = 1.5418$ Å). Spectra were collected

at room temperature in the range of $2\theta = 5°–80°$, with a step size of 0.05° and an acquisition time of 1 s for each point.

Scanning electron microscopy (SEM) images were obtained on a Hitachi S-5200 microscope with a field emission gun, using accelerating voltages from 2 to 5 kV.

FT-IR spectra were recorded using the KBr pellet technique on PERKIN-Elmer spectrometer in the range 4,000–400 cm^{-1} using a resolution of 4 cm^{-1}.

The calcined samples were analyzed by temperature programmed reduction (TPR) experiments which were done on a H$_2$ (5 %)/Ar mixture (50 ml/min) from room temperature up to 900 °C, with a heating rate of 10 °C/min. A thermal conductivity detector (TCD), previously calibrated using CuO, was used to evaluate the H$_2$ consumption. Experimental conditions were adjusted in order to avoid peak coalescence [29].

Catalytic activity

Catalytic activity tests were carried out in a quartz tubular down-flow reactor. Dimensions of the fix-bed reactor were 9 mm inner diameter and 16 cm long. The catalyst was placed in the middle of the reactor between two pompons of quartz wool. The reaction temperature was measured in the middle of the reactor by means of a K-type thermocouple. Feedstock gases were fed to reactor by independent mass flow controllers (Bronkhorst). The CH$_4$ and CO$_2$ reactants were mixed diluted in He (CH$_4$:CO$_2$:He = 10:10:80 in vol.). The sample was put in contact with the reaction mixture, and heated from room temperature up to 750 °C at 1 °C/min rate, holding the samples at 750 °C for 8 h. Prior to reaction conditions, all catalysts were treated "in situ" with a H$_2$ (5 %)/Ar mixture (50 ml/min) during 1 h at the same temperature of reaction (750 °C). Finally, the reaction was cooled down to room temperature in the same reaction mixture. In all the cases, the experiments have been carried out using a gas hourly space velocity (GHSV) of 300,000 L/kg h (20 mg of sample). Analysis of reactants and products were done by a Gas Chromatograph (Varian CP-3800) with a thermal conductivity sensor and a column (Porapak Q).

Results and discussion

Characterization of samples

The element chemical analysis results attached by ICP-AES are given in Table 1. As shown, composition of the samples are near the nominal ratios (M^{2+}/M^{3+} = 2), which confirms the quantitative precipitation of precursor salts.

The specific surface (S$_{BET}$) areas determined from N$_2$ adsorption/desorption isotherms using the BET method are also presented in Table 1. The N$_2$ adsorption/desorption isotherms for all the samples displayed type IV isotherms with clear hysteresis loops coming from the capillary condensation in mesopores. N$_2$ adsorption isotherms of this type are usually observed on mesoporous materials

Table 1 Chemical composition and specific surface area of samples

Samples	Relative metal composition	M^{2+}/M^{3+}	S_{BET} (m²/g)		
			Precursor	Calcined	Reduced at 750 °C
NiAl	$Ni_{0.66}Al_{0.34}$	1.94	68	114	65
NiMgAl	$Ni_{0.36}Mg_{0.32}Al_{0.32}$	2.12	96	101	100
NiCe	$Ni_{0.66}Ce_{0.34}$	1.94	176	41	18
NiMgCe	$Ni_{0.36}Mg_{0.34}Ce_{0.31}$	2.25	117	20	13

with no or few micropores and strong interaction between adsorbent and adsorbate molecules [30].

Calculations of the pore sizes in the samples using BJH method showed that these mesoporous materials present pore sizes widely distributed around 6–13 nm. The hysteresis loops observed in presence of calcined samples, are very similar to that obtained for precursors.

Surface areas of "as-synthesized" samples prior to calcination step shown relatively high S_{BET} values, between 68 and 176 m²/g. Incorporation of cerium resulted in an increase in the surface area, (68–176 m²/g, for NiAl → NiCe samples and from 96 to 117 m²/g for NiMgAl → NiMgCe). However, calcination of the "as prepared" samples resulted in notorious changes in the BET: while NiAl and NiMgAl, the specific surface area increases after calcination (68–176 m²/g, for NiAl and from 96 to 117 m²/g for NiMgAl), Ce-containing samples (NiCe, NiMgCe) decrease dramatically their specific surface area, (176–41 m²/g for NiCe and from 117 to 20 m²/g for NiMgCe). The increase of BET surface area on the Al containing samples (NiAl, NiMgAl) can be explained by the removal of water and carbonate as CO_2 from the interlayer space of the hydrotalcite structures, leading to structural breakdown [31], while the decrease of the BET surface area on the Ce containing samples (NiCe, NiMgCe) not formed the hydrotalcite structure can be ascribed to the formation and location of the CeO_2 species in the superficial porosity of the particles after thermal treatment [25].

Indeed, data shown in Table 1 reflect that specific surface areas of Al^{3+}-containing samples (NiAl, NiMgAl) are higher than those of Ce^{3+} containing samples (NiCe, NiMgCe), in good agreement with conclusions made by Cantrell et al. [32] who stipulated that samples rich in (Al^{3+}) lead to a higher content of compensating anions, which favor more open porosity after thermal treatment, leading to a higher surface area.

The XRD measurements of the precursors and XRD of mixed oxides obtained after the calcination step are shown in Fig. 1. Results from Fig. 1a confirm the formation of the precursor layered double hydroxide on Al-containing samples (NiAl, NiMgAl) as the diffraction profile showed the typical signals of the carbonated phase of the hydrotalcite structure [33]. That is not the case for the cerium containing samples (NiCe, NiMgCe), where poorly resolved diffractograms were observed. This could probably be caused by the Ce^{3+} cations, which cannot occupy the octahedral interstices in the cationic layers that constitute LDH structure

[34] due to their larger cationic radius [19, 28, 35]. Instead, these samples exhibit peaks typical of $CeCO_3OH$ (cerium hydroxycarbonate) together with CeO_2 [28].

XRD diagrams of samples calcined at 800 °C are presented in Fig. 1b. As can be seen, after thermal treatment, the hydrotalcite structure of the Al-containing samples was destroyed. On the NiAl sample, XRD patterns showed only the formation of NiO species. Consequently, an amorphous aluminum oxide phase should be also formed (not detected in XRD). NiMgAl diffractograms also present these peaks corresponding to NiO and amorphous Al_2O_3 phases, but a minority amount of $MgAl_2O_4$ (spinel type phase) is also detected. Nevertheless, considering the intensity and positions of the peaks in the diffractograms of NiMgAl and the broad peaks found, it should be remarked that some other possible phases could be also assigned, such as NiMgO, as most of the peaks of the NiMgO spinel are coincident with the NiO diffraction peaks. In this context, it has been already reported that the coprecipitation of Ni^{2+}, Mg^{2+} and Al^{3+} can generate solid solutions such as that proposed (NiMgO) after thermal activation due to the similar ionic sizes of cations [36].

On the other hand, XRD patterns of Ce-containing samples present similar peaks for both samples. These peaks correspond to NiO and CeO_2 species. Notwithstanding, as mentioned before in the case of the sample NiMgAl, the presence of a solid solution Mg–Ni–O on the NiMgCe catalyst cannot be excluded (present as an amorphous phase).

A detailed analysis of the broadening of the peaks, using the Scherrer formula, allowed the calculation of nanocrystal sizes of the different phases present in the samples. Sizes calculated are presented in Table 2.

The crystalline size of the NiO phase obtained for the Al-containing samples were notably smaller than those obtained for the Ce-containing samples. Al-containing samples showed NiO sizes values between 6 and 9 nm, meanwhile, NiO crystals in the Ce-containing samples showed sizes around 20 nm.
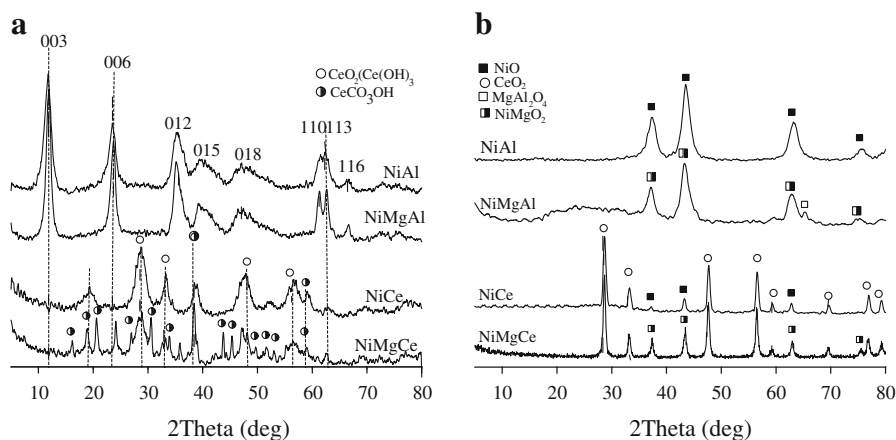
Fig. 1 XRD diagrams of co-precipitated precursors (a) mixed oxides (b)

**Table 2** Particle size, hydrogen consumption in TPR experiments

Samples	H_2 consumption (μmol/g)	XRD crystallite size (nm)					
		Calcined		Reduced at 750 °C		Used	
		NiO	CeO_2	Ni^0	CeO_2	Ni^0	CeO_2
NiAl	9,031	09	–	28	–	37	–
NiMgAl	5,232	06	–	17	–	31	–
NiCe	6,096	20	23	26	35	57	38
NiMgCe	886	24	24	nd	47	nd	48

nd not determined due to the low intensity of the signal

The TPR profiles obtained for all the samples are plotted in Fig. 2. The TPR of NiAl showed a profile with a main peak at 770 °C, preceded by a shoulder at ca. 600 °C. Also, a minor shoulder can be seen at 490 °C. According to the literature [37], the temperature of reduction of this minor shoulder could be attributed to reduction of NiO weakly interacting with the support. It is well known that the species that reduce at higher temperatures may correspond to Ni^{2+}, with high interaction with the surface or forming a solid solution with the support [38]. In this context, Ni-aluminates are claimed to be reduced at temperatures around 800 °C [39]. The NiCe reduction profile presents two main reduction peaks at ca. 420 and 500 °C and broad one at ca. 800 °C. This reduction profile is quite different compared with those obtained in previous works for samples Ni/CeO_2, where only one main peak appeared at about 390 °C, temperature slightly bellow of that necessary to reduce a commercial NiO (reduction peak at 420 °C) [40]. According to this, the species that reduced at 420 °C probably corresponds to NiO species weakly associated with the surface. The high temperature reduction peak may correspond to the surface and bulk reduction of CeO_2 according to previous reports that indicate that CeO_2 reduction occurs in two stages: the first one corresponding to the reduction of superficial oxygen between 480 and 500 °C, and the second one to the reduction of oxygen in the crystalline network between 780 and 800–900 °C [41].

The incorporation of Mg in the formulation of NiAl sample produces significant modifications in the reduction profiles. So, TPR of NiMgAl catalyst showed one main reduction peak with a maximum at around 810 °C indicating the existence of one single type of reducible species, which may correspond to the reduction of Ni^{2+} forming a solid solution with Mg and-or Al. So, no NiO phase is detected in the presence of Mg. Al^{3+} replacement by Ce^{3+} to obtain the NiMgCe sample produces also dramatic changes, leading to an almost flat profile, with just a weak and broad peak at 800 °C that can be ascribed to reduction of lattice oxygen atoms in the CeO_2. It is important to note that, if compared with NiCe sample, the incorporation of Mg results in the inexistence of any Ni^{2+} reduction process, which may only be ascribed to the formation of a solid solution NiMgO, that it is already known to hardly reduce below 1,000 °C [42].

Fig. 2 TPR profiles of mixed oxides
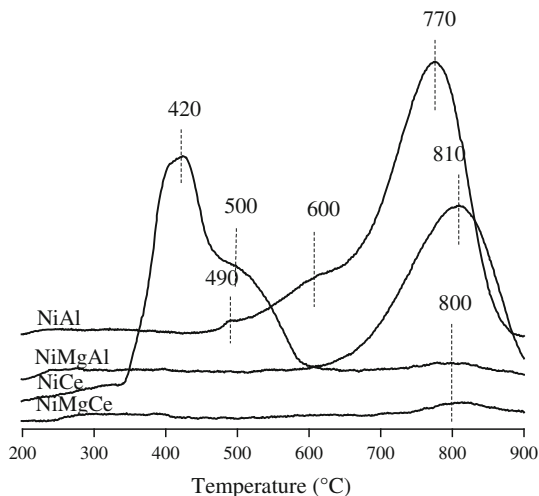
The TPR-H_2 technique is a quantitative method that allows us to find the amount of reducible species of a material. The H_2 consumptions, expressed in μmol/g of catalyst are detailed in Table 2. In both (NiAl, NiMgAl) samples, the consumptions correspond to that expected for the reduction of all the Ni(II) species to metallic Ni^0 species. In the case of NiCe sample an amount of hydrogen equal to that needed for reducing Ni(II) to Ni^0 is observed but, some excess of hydrogen is observed which could correspond to the surface reduction of the CeO_2, as discussed elsewhere [41, 43].

No significant consumption was measurable in the case of NiMgCe until 900 °C (only similar to that corresponding to CeO_2 bulk reduction in NiCe), showing that nickel is hard to reduce when forming a mixed oxide with cerium and magnesium.

Therefore, this TPR study shows that reducibility varies according to the following sequence: NiCe > NiAl > NiMgAl ≫ NiMgCe, which must be related with the interaction between nickel and Mg^{2+}/Ce^{4+} in the calcined catalysts, formed during decomposition step of precursors [25].

FT-IR spectroscopy can give useful information about the structure of the compounds and inter-lamellar anions. The FT-IR spectra of the samples previous calcination step are shown in Fig. 3a. In general, these spectra are typical of the LDH structure with interlayer carbonates anions [44]. All samples showed broad bands in the range 3460–3530 cm^{-1} due to the stretching mode of structural –OH groups in the metal hydroxide layer. A small shoulder at 2900–3000 cm^{-1} suggests the presence of a second type of –OH stretching vibration, possibly due to hydrogen bonding with carbonate in the interlayer spacing [35]. The shoulder at 1650 cm^{-1} may be ascribed to the bending mode of interlayer water molecules [45].

A sharp component at 3645 cm^{-1} is also found only for the samples containing cerium. This feature corresponds to that found on both $Ce(OH)_3$, an hydrotalcite-like impure hydroxide and $CeCO_3OH$, phases detected previously by XRD. The strong band at 1384 cm^{-1} is attributed to the carbonate anions. The shoulder close to 1500 cm^{-1} is due to the decreased symmetry of anions on samples containing
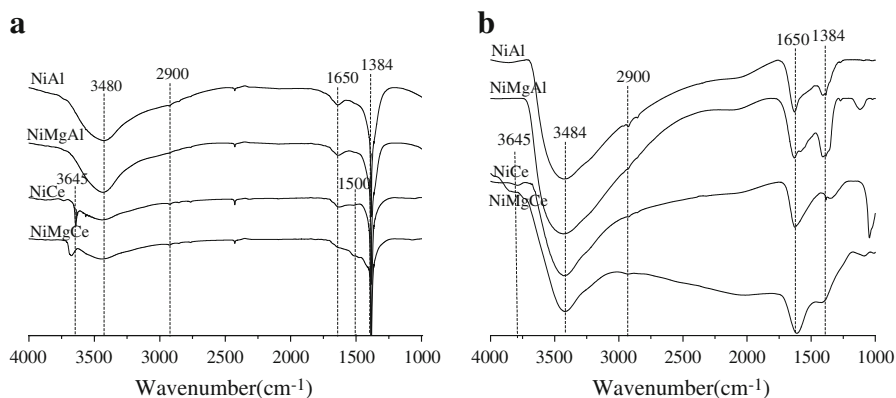
Fig. 3 FT-IR spectra of co-precipitated precursors (**a**) mixed oxides (**b**)

cerium. So, interestingly, this FT-IR results show that, even in the Ce-containing samples, where no hydrotalcite phase can be detected by XRD, an almost amorphous phase, similar to hydrotalcite remain in the as-prepared samples.

The FT-IR spectra of calcined catalysts are shown in Fig. 3b. Thermal decomposition of samples induced formation of mixed oxides although trace amounts of remaining carbonate was found in the spectra of all calcined samples (band at 1384 cm^{-1}). Although absorption bands at 3480 and 1650 cm^{-1} (present in all spectra) indicate the presence of OH^{-} and/or water, we should recall that dehydroxylation of samples is complete at applied calcinations temperature (400–450 °C).

The morphology of Ni based samples was investigated by SEM. As it can be seen in Fig. 4, the SEM image for NiAl reveals a solid that is composed by crystals with irregular shapes and well defined corners. NiMgAl shows a morphology that is slightly different from NiAl sample, also composed of grains of undefined forms but without specific morphology. Likewise, NiCe solid is mostly composed of smaller grains with irregular shapes. On the contrary, in the NiMgCe sample, two different kinds of particles can be observed. Energy dispersive X-ray analysis (EDX, Fig. 5) confirms that the big ones correspond to CeO$_2$ and the small ones correspond to solid solution of magnesium and nickel oxide.

Characterizations of the reduced catalysts

It is important to recall that in these catalysts, Ni should be in its metallic form (Ni^{0}) to be active for dry reforming of methane reaction. Therefore, we have accomplished a characterization of morphology and particle size distribution after the catalysts were reduced at 750 °C. SEM images of the reduced catalysts are shown in Fig. 6. For NiAl and NiMgAl samples, small bright particles, well formed, defined and homogeneously distributed over the support, can be clearly observed. Using STEM and Backscattering images, these particles have been confirmed to correspond to metallic nickel (Ni^{0}). The average size is between 15 nm and 25 nm
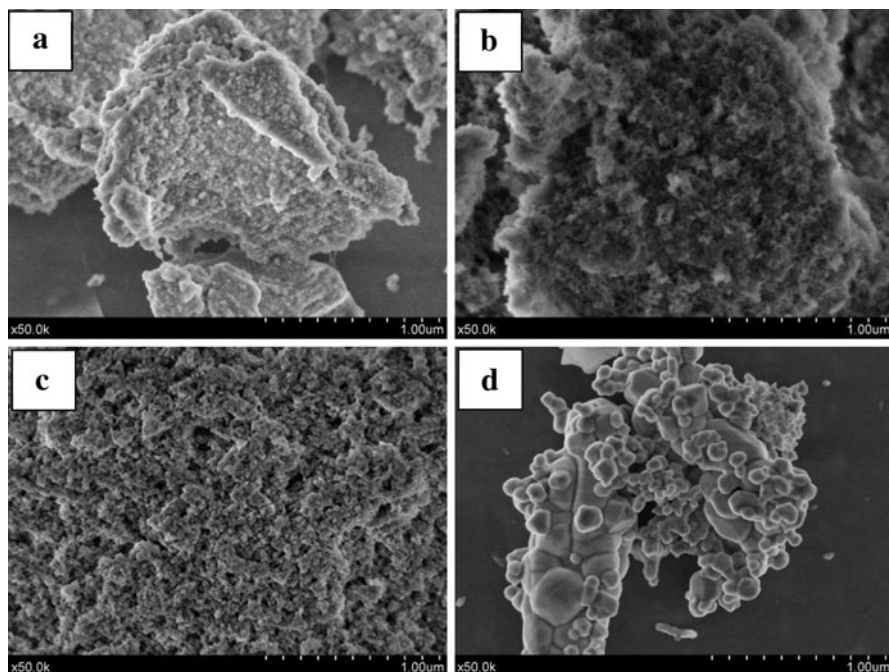
Fig. 4 Microscope images of mixed oxides: NiAl (**a**), NiMgAl (**b**), NiCe (**c**), NiMgCe (**d**)

(for NiMgAl and NiAl, respectively), values nearly equal to those given by XRD calculations. In the case of Ce containing samples Ni^0 particles with an average size of ca 20-25 nm are visible for NiCe while in the case of NiMgCe those particles were difficultly observed, suggesting that in this case Ni has not been reduced from its Ni^{2+} state in the Mg-Ni–O solid solution, in agreement with the previous TPR results.

The XRD patterns obtained after reduction at 750 °C show the presence of Ni^0, CeO_2 and/or NiMgO phases, as indicated in Fig. 7. CeO_2 and Ni particles sizes were calculated from these XRD diagrams by the Scherrer equation and also reported in Table 2. The average of the Ni^0 particles sizes obtained after reduction at 750 °C were between 17 and 28 nm.

After reduction, a small increase of NiO/Ni^0 particle sizes was observed for NiCe sample, much more severe for NiMgAl and especially NiAl. Although no Ni^0 is found in the NiMgCe reduced sample, it is interesting to remark that the NiO peaks present in the calcined sample have almost disappeared, pointing out that the reduction step has induced a deeper mixing of the NiO phase into the NiMgO structure.

In Table 1, BET values of the reduced samples are also incorporated. These values now vary from 13 to 100 m^2/g, indicating a decrease of specific surface area of ca. 50 %. Only the NiMgAl sample remains unchanged. The decrease in the surface area is in accordance with a general sintering of nanoparticles forming the catalysts, which seems to be more resistant to this agglomeration process in the
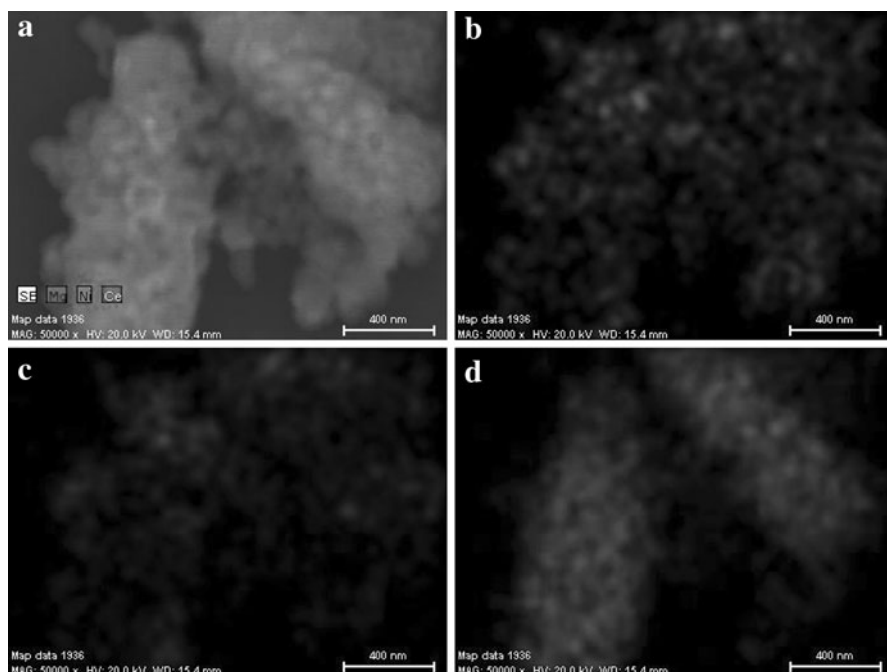
Fig. 5 EDX mapping of NiMgCe (**a**), Nickel (**b**), Magnesium (**c**), Cerium (**d**)

NiMgAl sample. Maybe, this effect is related to the presence of a more homogeneous solid solution, as endorsed by the single peak in the TPR profile of this sample (Fig. 2).

Catalytic activity

The catalytic performances of the different catalysts for CO_2 reforming of methane were evaluated at a reaction temperature of 750 °C, after an "in situ" H_2 reduction at 750 °C for 1 h. As expected, the main products from this reaction were H_2 and CO. The variations of CH_4 and CO_2 conversions versus time on stream are presented in Fig. 8. Selectivity (expressed as CH_4 conversion/CO_2 conversion ratio) is shown in Fig. 9. The first feature that can be readily drawn is that the performances levels of the catalysts remains constant after 8 h of reaction time, indicating that no perceptible deactivation took place within this period. If we focus on the CH_4 conversion, we could say that catalysts NiMgAl (ca. 94 %)—a value near thermodynamical equilibrium—and NiCe (85 %) show the highest performance, followed by NiAl (65 %), being the NiMgCe samples the one with the lowest conversion (45 %). The conversion for CO_2 shows a similar tendency.

Fig. 9 shows H_2/CO ratios obtained at 750 °C, in presence of Ni based-catalysts. This figure is a direct consequence of the differences in the conversion levels of CH_4 and CO_2. Once again, the value of the H_2/CO ratio remains approximately constant for all the catalysts after 8 h on stream. For NiMgAl and NiCe catalysts, the H_2/CO
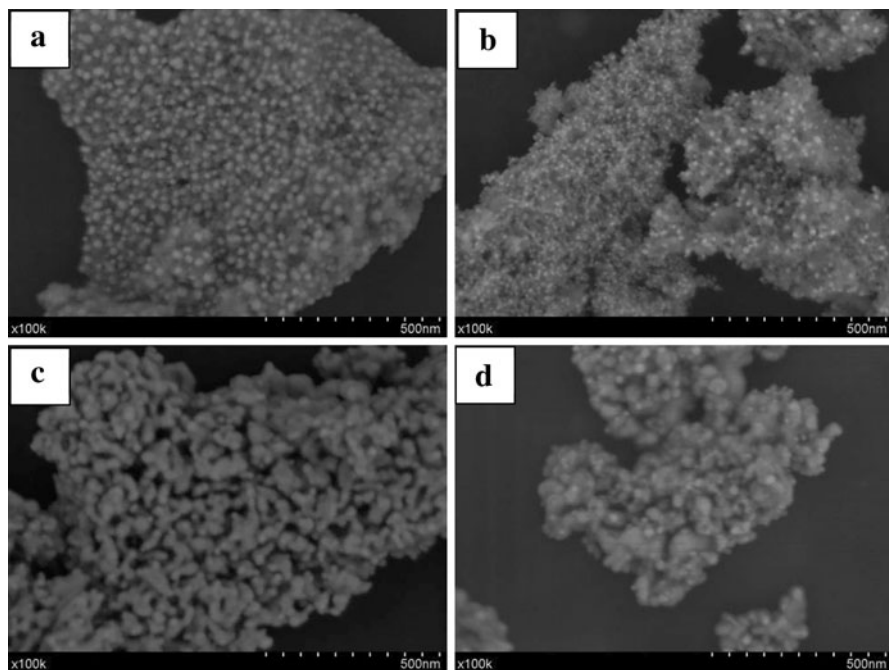
**Fig. 6** Microscope images of reduced catalysts at 750 °C: NiAl (**a**), NiMgAl (**b**), NiCe (**c**), NiMgCe (**d**)


Fig. 7 XRD of reduced catalysts at 750 °C
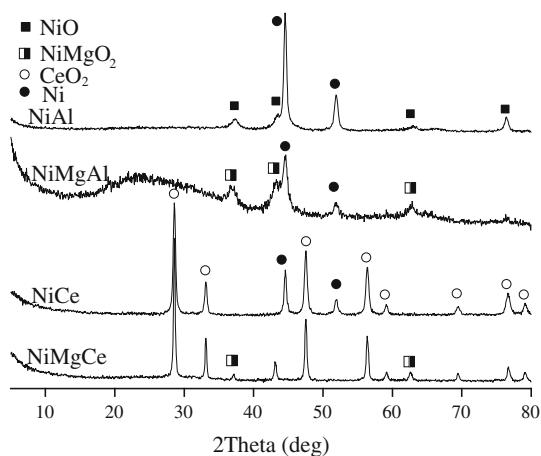
ratio is almost that corresponding to the thermodynamic equilibrium (ca. 1.0). On the other hand, NiAl and NiMgCe show a H_2/CO ratio smaller than unity. The deviation from the stoichiometric ratio, mainly in the NiAl case, reflects the occurrence of the reverse water–gas shift reaction [46].

We can try to summarize and discuss the results on terms of the effect of substitution/incorporation of Al by Ce and/or Mg. In this context, the NiAl catalyst
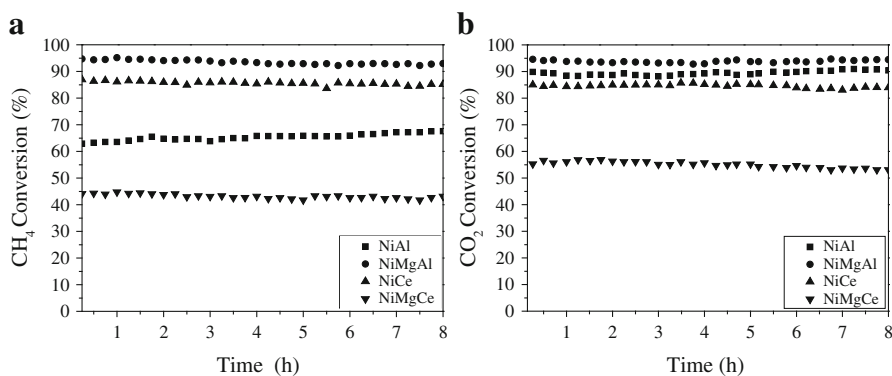
Fig. 8 CH$_4$ (**a**) and CO$_2$ (**b**) conversions evolution versus time on stream for Ni-catalysts (750 °C, $P = 1$ atm, CO$_2$/CH$_4$ = 1, GHSV = 300,000 l/kg$_{cat}$ h)

Fig. 9 Selectivity evolution, H$_2$/CO ratio versus time on stream for Ni-catalysts (750 °C, $P = 1$ atm, CO$_2$/CH$_4$ = 1, GHSV = 300,000 l/kg$_{cat}$ h)
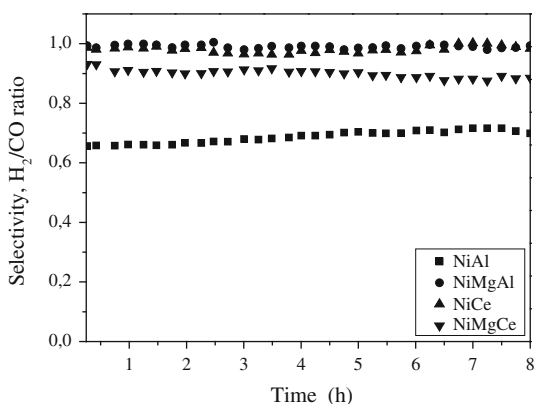
displayed a moderate activity towards dry reforming of methane (65 %) and also a moderate selectivity (H$_2$/CO ratio), far from the thermodynamic conditions (ca. 90 % conversion and H$_2$/CO = 1.0). The incorporation of Mg, resulting in NiMgAl catalysts, leads to a substantial increase in the reactants conversions (ca 94 %), as well as in the H$_2$/CO ratio (0.98).

In summary, the observed order of methane conversions is: NiMgAl > NiCe > NiAl ≫ NiMgCe, while the selectivity follows the trend NiMgAl > NiCe > NiMgCe >>> NiAl.

First of all, the lower performance observed for the NiMgCe can be related to the lack of reducibility at low temperature. So, the absence of a completely reduced nickel phase, which forms a NiMgO solid solution, would explain its worse performance.

On the other hand, the best catalytic performance of the system NiMgAl, seems to be related with two different factors. First, the high stability of the support, maintaining a very high specific surface (ca. 100 m^2/g), after the reducing treatment. This stability could be related with the formation of a very

homogeneous NiMgO solid solution, as endorsed by the single peak in the TPR profile (Fig. 2). This phase produces after reduction a well dispersed metallic nickel (SEM image in Fig. 6), strongly interacting with the support. Alternatively, it cannot be excluded that the presence of a basic cation like Mg^{2+} can reduce the deposition of harmful coke carbon, improving the stability of the catalyst performance [47, 48].

In the case of the NiCe sample, its high performance, between the NiAl and NiMgAl samples could be related with the well known effect of cerium in catalytic performance due to the redox character of this oxide ($CeO_{2-x} \leftrightarrow CeO_2$) as electron transfer reactions increase the inhibition potential towards the carbon formation in the catalyst. Xu and al [49] affirm that during CO_2 reforming process, CO_2 is adsorbed on the basic or redox centers (oxygen vacancies in CeO_{2-x}) and there, it produces CO and CeO_2 in a redox cycle. Afterwards, the CeO_2 reacts with the carbon deposited by dehydrogenization of the C–H bond and oxidation to produce CeO_{2-x} and CO_2 again. That mechanism can also explain the increase of the total basicity of mixed oxides doped with Ce, given the adsorption of CO_2 that can occur in the anionic vacancies of CeO_2. In the same context, it was reported that a strong interaction of nickel particles with CeO_2 support improves the catalytic performance of Ni–Ce sample during the reaction [50]. It should be remarked that NiCe present a particle size similar to that of the NiAl sample, although in this case the NiCe present a better reducibility (in terms of lower temperature to complete the reduction).

Characterizations of used catalysts

In order to follow the possible microstructural changes in the support and active phase (Ni) as well as the coke deposition (carbon formation), the Ni-catalysts tested for reactivity were removed after 8 h of reaction time on stream, and characterized with XRD and SEM. The results of XRD measurements of used catalysts are shown in Fig. 10. In the Ce containing samples, the XRD diagrams show narrow peaks for

Fig. 10 XRD diagrams of used catalysts
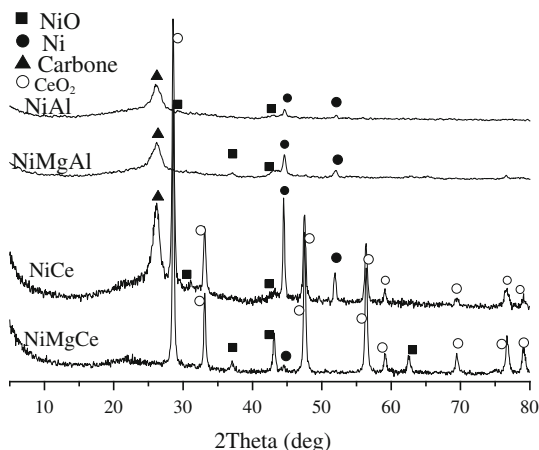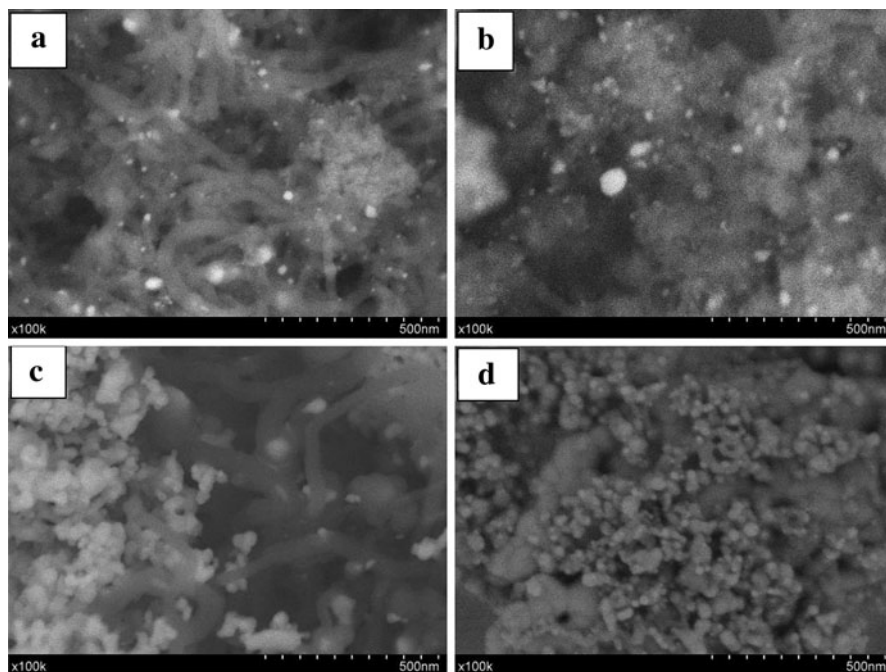
Fig. 11 Microscope images of used catalysts: NiAl (**a**), NiMgAl (**b**), NiCe (**c**), NiMgCe (**d**)

both CeO_2 and Ni phases. Calculation of crystallite size, using the Scherrer formula, indicates almost no modification in the CeO_2 phase, but a significant increase in the Ni^0 particle size for NiCe sample (see Table 2). In the case of NiMgCe, Ni remains as an oxidized phase. In the Al containing samples (NiAl, NiMgAl), the diagrams show very broad peaks, with no detectable peaks for the support and small peaks assigned to Ni^0, and tiny shoulder that seems to indicate the presence of NiO. The peaks at $\theta = 27°$ correspond to the formation of carbon for NiAl, NiMgAl and NiCe, and its absent for NiMgCe. It is important to point out that XRD signals characteristic of some types of coke deposited on the surface are not observed in general.

A SEM study of post-reaction samples is presented in Fig. 11. From these images, it is clear that after dry reforming reaction, the carbon detected on catalysts NiMgAl, NiAl and NiCe is in the form of nano-fibers. The presence of this type of carbon may help to explain why these catalysts do not deactivated even after 8 h on stream, opposite to what is expected if coke or C_xH_y carbon occurs. Noteworthy is the absence of any carbon traces in the NiMgCe case, in accordance with XRD results. Moreover, the NiMgAl catalyst present also very high activity and stability even under concentrated conditions. Nevertheless, we have noticed that this catalyst produced a considerable amount of carbon nano-fibers under operating conditions, although this type of carbon do not seem to induce a deactivation of this catalyst.

Conclusions

Different catalysts containing Ni/Mg/Al/Ce oxides have been prepared by the thermal decomposition of mixed oxides with related hydrotalcites structures. It was shown that the incorporation of cerium by coprecipitation does not involve the isomorphic substitution of Ce^{3+} in the NiAl hydrotalcites systems. This could probably be caused by the difference in ionic sizes, when Ce^{3+} ions are incorporated to the synthesis, no crystalline hydrotalcite structure are obtained.

The best catalytic results for the dry reforming of methane have been obtained with the NiMgAl solid, where the values of conversion and selectivity were near the thermodynamic equilibrium at 750 °C. This high performance can be explained considering the presence of a very homogeneous Ni/Mg/O solid solution, yielding after hydrogen reduction a catalyst with a very high and stable specific surface, with tiny Ni^0 particles homogeneously dispersed on the support. Although less active, the NiCe system also presents a high performance, probably due to the redox properties of the cerium oxide phase, which affects the adsorption properties of CO and the reactivity of carbon deposits. Finally, in the NiMgCe sample, a very stable and poorly reducible mixed oxide phase is formed, which inhibits its catalytic performance.

References

1. Tsyganok AI, Suzuki K, Hamakawa S, Takehira K, Hayakawa T (2001) Catal Lett 77:75–86
2. Batiot-Dupeyrat C, Sierra GA, Mondragon F, Barrault J, Tatibouet JM (2005) Catal Today 474:107–108
3. Lemonidou AA, Vasalos IA (2002) Appl Catal A 228:227–235
4. Martinez R, Romero E, Guimon C, Bilbao R (2004) Appl Catal A 274:139–149
5. Zhan Y, Li D, Nishida K, Shishido T, Oumi Y, Sano T, Takehira K (2009) Appl Clay Sci 45:147–154
6. Takehira K, Shishido T, Wang P, Kosaka T, Takaki K (2004) J Catal 221:43–54
7. Rostrup-Nielsen JR, Sehested J, Norskov JK (2002) Adv Catal 47:65–139
8. Takheira K (2002) Catal Surv Japan 6:19–32
9. Araujo GC, Lima SM, Assaf JM, Pena MA, Fierro JLG, Rangel MC (2008) Catal Today 133:129–135
10. Shishido T, Sukenobu M, Morioka H, Furukawa R, Shirahase H, Takehira K (2001) Catal Lett 73:21–26
11. Vaccari A (1998) Catal Today 41:53–71
12. Tsyganok AI, Tsunoda T, Hamakawa S, Suzuki K, Takehira K, Hayakawa T (2003) J Catal 213(2):191–203
13. Takehira K (2009) J Nat Gas Chem 18:237–259
14. Li D, Nishida K, Zhan Y, Shishido T, Oumi Y, Sano T, Takehira K (2009) Appl Clay Sci 43:49–56
15. Hou Z, Yashima T (2004) Appl Catal A 261:205–209
16. Takehira K, Shishido T, Shoro D, Murakami K, Honda M, Kawabata T, Takaki K (2004) Catal Commun 5:209–213
17. Wang N, Chu W, Zhang T, Zhao XS (2012) Int J Hydrogen Energy 37:19–30
18. Yu X, Wanga N, Chu W, Liu M (2012) Chem Eng J 209:623–632
19. Vizcarno AJ, Lindo M, Carrero A, Calles JA (2012) Int J Hydrogen Energy 37:1985–1992
20. Bae JW, Kim AR, Baek SC, Jun KW (2011) Reac Kinet Mech Cat 104:377–388
21. Munoz M, Moreno S, Molina R (2012) Int J Hydrogen Energy 37:18827–18842
22. Kim DK, Stöwe K, Müller F, Maier WF (2007) J Catal 247:101–111

23. Centeno MA, Paulis M, Montes M, Odriozola JA (2002) Appl Catal A 234:65–78
24. Daza CE, Gallegob J, Andre J, Moreno S, Mondrago F, Moreno S, Molina R (2008) Catal Today 133–135:357–366
25. Daza CE, Gallego J, Mondragon F, Moreno S, Molina R (2010) Fuel 89:592–603
26. Daza CE, Moreno S, Molina R (2010) Catal Commun 12:173–179
27. Daza CE, Cabrera CR, Moreno S, Molina R (2010) Appl Catal A 378:125–133
28. Daza CE, Moreno S, Molina R (2011) Int J Hydrogen Energy 36:3886–3894
29. Malet P, Caballero A (1988) J Chem Soc I(84):2369–2375
30. Wu GD, Wang XL, Chen B, Li JP, Zhao N, Wei W (2007) Appl Catal A 329:106–111
31. Holgado MJ, Rives V, San Raman S (2001) Appl Catal A 214:219–228
32. Cantrell DG, Gillie LJ, Lee AF, Wilson K (2005) Appl Catal A 287:183–190
33. Rives V (2002) Mater Chem Phys 75:19–25
34. Melo F, Morlane N (2008) Catal Today 133–135:374–382
35. Das J, Das D, Parida KM (2006) J Colloid Interface Sci 301:569–574
36. Tsyganok AI, Inaba M, Tsunoda T, Hamakawa S, Suzuki K, Hayakawa T (2003) Catal Commun 4:493–498
37. Hai-Peng WU, Wen-jing LI, Li GUO, Yan-fei PAN, Xiu-feng XU (2011) J Fuel Chem Technol 39:550–555
38. Albertazzi S, Basile F, Benito P, Del Gallo P, Fornasari G, Gary D, Rosetti V, Vaccari A (2007) Catal Today 128:258–263
39. Sahli N, Petit C, Roger AC, Kiennemann A, Libs S, Bettahar MM (2006) Catal Today 113:187–193
40. Gonzalez-Delacruz VM, Ternero F, Pereníguez R, Caballero A, Holgado JP (2010) Appl Catal A 384:1–9
41. Holgado JP, Alvarez R, Munuera G (2000) Appl Surf Sci 161:301–315
42. Chen YG, Tomishige K, Yokoyama K, Fujimoto K (1997) App Catal A 165:335–347
43. Holgado JP, Munuera G (1995) Stud Surf Sci Catal 96:109–122
44. Cavani F, Trifiro F, Vaccari A (1991) Catal Today 11:173–301
45. Kloprogge JT, Frost RL (2001) In: Rives V (ed) Layered Double Hydroxides: Present and Future. Nova Science Publishers, New York, pp 139–192
46. Montoya JA, Romero-Pascal E, Gimon C, Del Angel P, Monzon A (2000) Catal Today 63:71–85
47. Djaidja A, Libs S, Kiennemann A, Barama A (2006) Catal Today 113:194–200
48. Tsyganok AI, Inaba M, Tsunoda T, Uchida K, Suzuki K, Takehira K (2005) Appl Catal A 292:328–343
49. Xu G, Shi K, Gao Y, Xu H, Wei Y (1999) J Mol Catal A 147:47–54
50. Gonzalez-DelaCruz VM, Holgado JP, Pereníguez R, Caballero A (2008) J Catal 257:307–314